JOURNAL OF SOLID STATE CHEMISTRY 114, 560–574 (1995)

Structural Studies on New Ternary Oxides $Ba_8Ta_4Ti_3O_{24}$ and $Ba_{10}Ta_{7.04}Ti_{1.2}O_{30}$

R. V. Shpanchenko,[1] L. Nistor,[2] G. Van Tendeloo, J. Van Landuyt,[3] and S. Amelinckx

EMAT, University of Antwerp (RUCA), Groenenborgerlaan 171, 2020 Antwerp, Belgium

and

A. M. Abakumov, E. V. Antipov, and L. M. Kovba

Department of Chemistry, Moscow State University, 119899 Moscow, Russia

Received April 7, 1994; in revised form June 27, 1994; accepted June 28, 1994

The ternary oxides $Ba_8Ta_4Ti_3O_{24}$ and $Ba_{10}Ta_{7.04}Ti_{1.2}O_{30}$ were synthesized and their crystal structures and defects were studied by means of X-ray powder diffraction, electron diffraction, and high resolution electron microscopy. The crystal structure of $Ba_8Ta_4Ti_3O_{24}$ is based on the $8H$ $(cchc)_2$ close-packed stacking (a = 10.0314 Å, c = 18.869 Å, SG $P6_3/mcm$, Z = 3) and that of $Ba_{10}Ta_{7.04}Ti_{1.2}O_{30}$ and on the $10H$ $(cchcc)_2$ close-packed stacking (a = 5.7981 Å, c = 23.755 Å, SG $P6_3/mmc$, Z = 1) of BaO_3 layers. The structural refinements gave the following values for the R factors for $Ba_8Ta_4Ti_3O_{24}$ ($Ba_{10}Ta_{7.04}Ti_{1.2}O_{30}$) R_I = 0.041 (0.039), R_P = 0.108 (0.118), and R_{wP} = 0.094 (0.099). The main feature of both structures is the presence of two types of face-sharing octahedra (FSO) with different occupancies by Ta atoms, Ti atoms, and vacancies, which results in the formation of a superstructure. It was shown that in the $Ba_8Ta_4Ti_3O_{24}$ structure these pairs of FSO occur in an ordered fashion and in the $Ba_{10}Ta_{7.04}Ti_{1.2}O_{30}$ structure in a disordered fashion. The existence of the wide range of solid solutions was shown to be also a consequence of the presence of one of the two types of face-sharing octahedra.

1. INTRODUCTION

The complex hexagonal perovskite-like oxides can be described in terms of the close-packing of AO_3 layers along the c-axis of the hexagonal cell, the B-cations being situated in the octahedral interstices. If the stacking sequence contains hexagonal triplets (h), chains of face-sharing octahedra (FSO) parallel to the c-axis must exist in the structure. The stability of such structures depends on the B-cation size and on the possibility of compensation of the electrostatic repulsion between the B-cations with large formal charges in adjacent octahedra. Such a compensation may occur in different ways, for example by the formation of metal–metal bonds as it is realized in the $BaRuO_3$ structure (1). The reduction of the electrostatic repulsion can also be achieved by the location of B-cations with small formal charges in the FSO. This leads to the formation of compounds like $Ba_4M_3LiO_{12}$ (M = Ta, Nb) (2) or $Ba_5W_3Li_2O_{15}$ (3) where both Li and M (M = W, Ta, Nb) atoms occupy the same crystallographic positions in the FSO. The same result can be obtained if the octahedral interstices are partially occupied by atoms with a large electrostatic charge and by cation vacancies. This possibility is realized in the crystal structure of $Ba_8M_4Ti_3O_{24}$ (M = Nb, Ta) (4), where the FSO are occupied by M and Ti atoms and by vacancies.

The aim of our work was the preparation of compounds with a statistical occupation of the singular crystallographic positions in the FSO by cations with high formal charge and by vacancies, and the determination of the B-cation distribution in the structures of these compounds. An electron microscopy study revealed the presence of a superstructure and confirmed the main features of the X-ray crystal structure determination of the basic structure.

2. EXPERIMENTAL

All studied samples were prepared by sintering techniques using $BaCO_3$, Ta_2O_5, and TiO_2 (previously dried at 400°C) as initial reagents. Stoichiometric mixtures of oxides were ground in an agate mortar under acetone followed by pressing into pellets. The samples were heated at 1050°C for 40 hr. After regrinding, they were pressed again followed by heat treatment at 1400°C for

[1] On leave from the Department of Chemistry, Moscow State University, 119899 Moscow, Russia.

[2] On leave from the Institute of Atomic Physics IFTM, P.O. Box Mg. 6, Bucharest, Romania.

[3] To whom correspondence should be addressed.

0022-4596/95 $6.00

60–70 hr. Synthesis were carried out in air in "Naberterm" furnaces and in furnaces with lanthanum chromite heaters in Al_2O_3 crucibles. The samples were finally furnace cooled.

The phase composition of the prepared samples and the lattice parameters of the compounds were determined using X-ray powder diffraction data obtained with a focusing Guinier FR-552 camera ($CuK\alpha_1$-radiation; germanium was used as an internal standard). Raw data for crystal structure determinations were collected using the STADI/P diffractometer ($CuK\alpha_1$-radiation, curved Ge-monochromator, transmission mode, step 0.02°(2θ), acquisition time 60 (sec/step), scintillation counter).

The crystal structure computations were carried out using the CSD program package (5). The Rietveld method with pseudo-Voigt profile functions was used for the final refinement. R_p and R_{wp} were calculated after the background was subtracted from the experimental data.

Samples for transmission electron microscopy investigations were prepared by crushing the pellets under alcohol and dispersing the grains on copper grids covered with a holey carbon film. A Philips CM-20 electron microscope with a double tilting stage was used for diffraction studies. High resolution images were obtained in a JEOL-4000EX electron microscope operating at 400 kV.

Quantitative X-ray analysis was performed with a CAMEBAX-MicroBeam system. Since the $K\alpha$-peaks of titanium strongly overlap the $L\alpha$-peaks of barium, the measurements were made on the $K\beta$ peaks of Ti and $L\beta$ of Ba. $Ba_9LaTa_7TiO_{30}$ oxide was used as a standard. Assuming the concentration of Ba and O atoms to be known from the 10-layer close-packing of the stoichiometric BaO_3 layers, the Ta and Ti concentrations could be determined. Measurements were performed for the sample with bulk composition $Ba_{10}Ta_{6.95}Ti_{1.35}O_{30}$.

3. RESULTS

3.1. Synthesis and X-ray Diffraction

As will be seen below, several syntheses were performed in order to obtain a better structural characterisation of these ternary oxides.

3.1.1. $Ba_8Ta_4Ti_3O_{24}$ Oxide. The X-ray diffraction pattern of the sample revealed $Ba_8Ta_4Ti_3O_{24}$; it was indexed on a hexagonal lattice with parameters a = 5.7913(1) Å, c = 18.8710(7) Å, z = 1. The eight-layered close-packed stacking of the BaO_3 layers is realized in the structure of $Ba_8Ta_4Ti_3O_{24}$. A crystal structure model with the symmetry D_{6h}^4 ($P6_3/mmc$) and a $(cchc)_2$ stacking sequence was chosen (as that suggested for $Ba_8Nb_4Ti_3O_{24}$, (4). Refinement of this model resulted in values of R_I = 0.040, R_P = 0.113, and R_{wp} = 0.110. However, since the electron diffraction study showed the existence of a superstructure further refinement was necessary.

$Ba_8Ta_4Ti_3O_{24}$ oxide has a wide range of homogeneity when Ti atoms are substituted by Ta atoms. As a result $Ba_8Ta_{4+0.8x}Ti_{3-x}O_{24}$ ($0 \leq x0.8$) solid solutions are formed. The lattice parameters slightly increase as x increases. For example, the cell parameters for $Ba_8Ta_{4.64}Ti_{2.2}O_{24}$ (x = 0.8) are a = 5.8038(9) Å, c = 18.912(5) Å. Two-phase samples were obtained for compositions outside the indicated range and the cell parameters of the compounds were equal to those of the extreme points of the solid solution range. These samples contained $Ba_8Ta_4Ti_3O_{24}$ and $BaTiO_3$ when $x < 0$. When $x > 0.8$, a new phase was found next to $Ba_8Ta_{4.64}Ti_{2.2}O_{24}$.

We also synthesized samples with compositions $Ba_8Ta_{4.64-x}Ti_{2.2+x}O_{24-x/2}$ in order to study the existence of both cation and anion vacancies in the structure. All the samples (except for x = 0) were polyphasic. This means that the composition of the BaO_3 layers is constant and does not depend on the composition of the B-framework.

3.1.2. $Ba_{10}Ta_{7.04}Ti_{1.2}O_{30}$ Oxide. The quantitative X-ray analysis gave a cation ratio for this new oxide: Ba : Ta : Ti = 21(2) : 15(2) : 2.4(3) which corresponds to the composition $Ba_{10}Ta_{7.04}Ti_{1.2}O_{30}$.

The X-ray diffraction pattern of this new compound (prepared with determined stoichiometry in a pure form) was also indexed on a hexagonal lattice (a = 5.7966(1) Å, c = 23.7482(7) Å), corresponding to a 10-layered close-packing.

Solid solutions with a general formula $Ba_{10}Ta_{8-0.8x}Ti_xO_{30}$ (isostructural with $Ba_{10}Ta_{7.04}Ti_{1.2}O_{30}$) were found in the range $0.6 \leq x \leq 1.2$. The cell parameters for these compounds decrease with increasing titanium content: they are a = 5.8056(5) Å, c = 23.860(3) Å (for x = 0.6) and a = 5.7966(1) Å, c = 23.7482(7) Å (for x = 1.2). When $x < 0.6$ the samples contained $Ba_{10}Ta_{7.52}Ti_{0.6}O_{30}$ and $Ba_5Ta_4O_{15}$.

The study of the series of solid solutions $Ba_8Ta_{4+0.8x}Ti_{3-x}O_{24}$ and $Ba_{10}Ta_{8-0.8x}Ti_xO_{30}$ did not reveal any differences in the diffraction patterns for different values of x. This means that no considerable structural changes occur during solid solution formation.

3.2. Electron Diffraction

3.2.1. $Ba_8Ta_4Ti_3O_{24}$ Oxide. The electron diffraction patterns for the most relevant zone axes are given in Fig. 1. The pattern along the $[0001]_b^*$ zone, where the subscript b refers to the basic cell (Fig. 1a), exhibits the geometry and the intensity distribution which are consistent with the structure of the BaO_3 layers: the first hexagon is less intense than the second one. The deduced lattice parameter a = 5.79 Å is consistent with that determined by X-ray diffraction for the basic cell. In the same diffraction pattern, the triangles of spots are centered by much weaker spots. These are the superstructure spots. Their

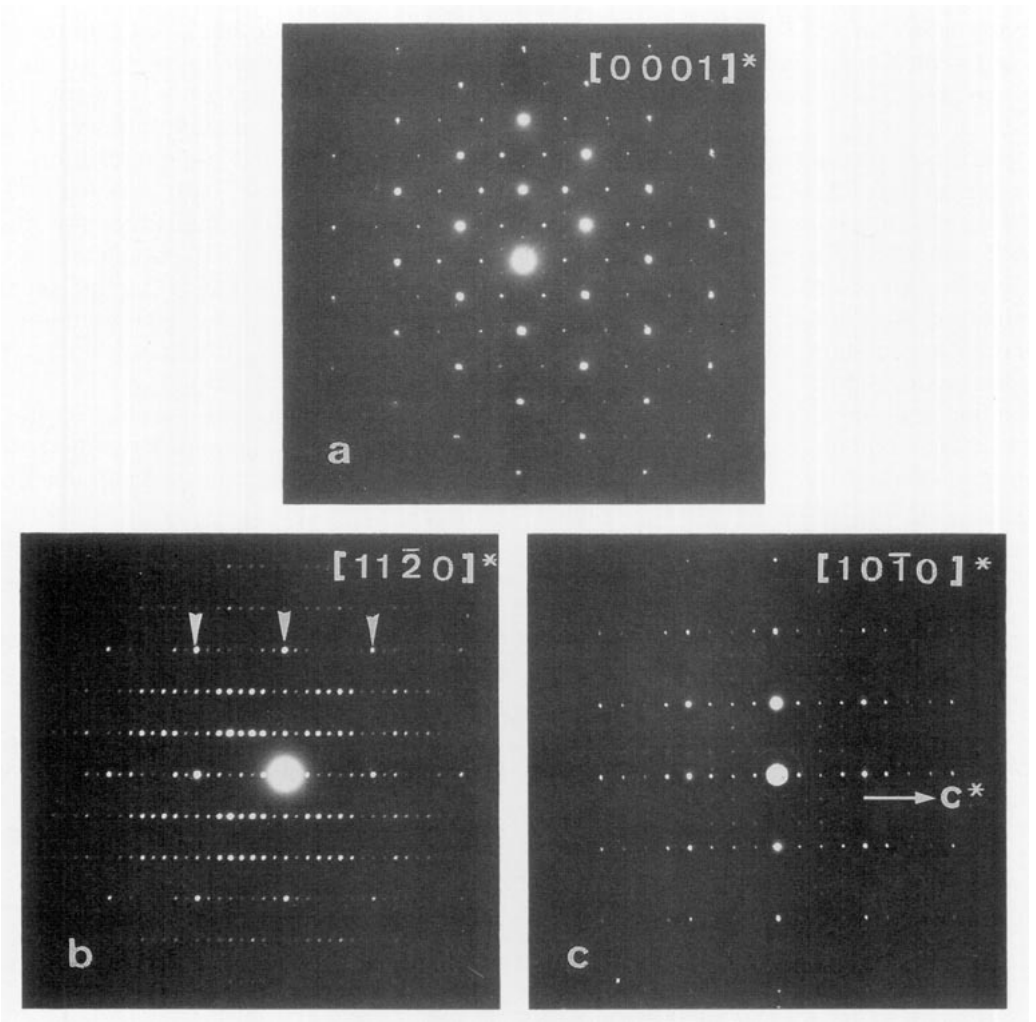

FIG. 1. Three sections of the reciprocal space of the basic structure of the $Ba_8Ta_4Ti_3O_{24}$ compound: (a) $[0001]_b^*$ zone; (b) $[11\bar{2}0]_b^*$ zone; (c) $[10\bar{1}]_b^*$ zone. Index b denotes the basic structure. Superstructure spots are evident in the (a) and (c) images.

presence leads to a $\sqrt{3}$ times increase in the a-parameter and to a rotation of the reference axes by 30°.

Thus the superstructure has a unit mesh in the (0001) plane given by the base vectors $\mathbf{a}_{1s}$ and $\mathbf{a}_{2s}$ related to the basic vectors $\mathbf{a}_{1b}$ and $\mathbf{a}_{2b}$ by the relation:

$$\begin{pmatrix} \mathbf{a}_{1s} \\ \mathbf{a}_{2s} \end{pmatrix} = \begin{pmatrix} 1 & -1 \\ 1 & 2 \end{pmatrix} \begin{pmatrix} \mathbf{a}_{1b} \\ \mathbf{a}_{2b} \end{pmatrix}.$$

From the $[11\bar{2}0]_b^*$ zone pattern (Fig. 1b) we deduced $c = 16.86$ Å, in agreement with the value found by X-ray diffraction. Along the $(000l)$ row of spots, the spots with $l = 2n + 1$ are systematically weaker than those with $l = 2n$.

The $[10\bar{1}0]_b^*$ zone is shown in Fig. 1c. The spots with $l = 2n + 1$ are systematically absent. This shows that the diffraction conditions are such that the $000l$ reflections are only present for $l = 2n$ and that also the $h\bar{h}0l$ reflections are only present for $l = 2n$. Therefore in the $[11\bar{2}0]_b^*$ zone pattern the $000l$ reflections with $l = 2n + 1$ must be attributed to double diffraction.

The superstructure spots seen in the $[0001]_b^*$ zone are also present in the $[10\bar{1}0]_b^*$ zone. The lattice vectors parallel to the $[11\bar{2}0]_b^*$ direction in the reciprocal space are divided in three equal parts by the superstructure spots and only $l = 2n$ spots are present.

The electron diffraction patterns suggest the following conditions:

$$000l \quad \text{for } l = 2n$$

$$h\bar{h}0l \quad \text{for } l = 2n.$$

Since no spots indicating an increase in the c-parameter were found, we chose $P6_3/mcm$ as space group for the

superstructure. The unit cell for the superstructure in direct space for $Ba_8Ta_4Ti_3O_{24}$ is represented in Fig. 2.

The $[11\bar{2}0]_b^*$ zone electron diffraction pattern deserves additional comments. It reflects the periodically twinned character of the BaO_3 framework, also visible in the high resolution images discussed below. The intensity of the spots along the rows $h = 3n$ is modulated except for $n = 0$, with a period equal to eight interspot distances. This long reciprocal period corresponds to one interlayer spacing of the BaO_3 framework. It corresponds to a unit cell with a height of eight times the interlayer spacing. The strongest spots in the rows $h = 3n$ form a rectangular lattice of which the unit mesh is indicated by arrows in Fig. 1b. The intensities of the spots in the rows $h = 3n \pm 1$ exhibit maxima close to the diagonals of this rectangle. Along these rows the diagonal intersects the spacing between successive spots in the ratio 1/3 : 2/3 in the rows $h = 3n + 1$ and in the ratio 2/3 : 1/3 in the rows $h = 3n - 1$. Such maxima in intensity occurring close to the diagonals of the rectangle suggest that the framework is periodically twinned. The geometry as well as the intensity distribution indicate a subunit cell twinned structure, according to (6). The absence of spacing anomalies further indicates that the twinning period is exactly eight unit layers spacing. The intensity distribution in the $h = 0$ row of spots is singular, because the spots with $l = 2n + 1$ are only present due to double diffraction.

3.2.2. $Ba_{10}Ta_{7.04}Ti_{1.2}O_{30}$ Oxide. A superstructure similar to that of $Ba_8Ta_4Ti_3O_{24}$ was found for $Ba_{10}Ta_{7.04}Ti_{1.2}O_{30}$. The electron diffraction patterns of the $[0001]_b^*$, $[11\bar{2}0]_b^*$, and $[10\bar{1}0]_b^*$ zones are shown in Fig. 3. The main difference, apart from a change of the lattice parameters, was along the $[1010]^*$ zone, where only streaking suggests considerable disorder in the superstructure, as compared to the well-ordered $Ba_8Ta_4Ti_3O_{24}$ phase. The streaks appeared as lines of diffuse intensity parallel to the c^* direction at positions in the reciprocal space where rows of discrete spots were found in the diffraction pattern of the $Ba_8Ta_4Ti_3O_{24}$ compound. Tilting experiments revealed that no superstructure spots are visible in the exact basal section, but that spots appear in slightly tilted orientations, due to the intersections of the Ewald's sphere with these lines. The streaks are intensity modulated, the period of the modulation being the inverse of the separation between successive BaO_3 layers. The "phase" of the modulation is such that for $l = 0$ the intensity is a minimum. Such streaks are due to one-dimensional disorder in the ordered two-dimensional arrangement of cations and vacancies within the hexagonal triplet of BaO_3 layers. Since the BaO_3 framework does not contribute to the diffracted intensity along these lines, the modulation must be related to the disorder associated with the ordering pattern in layers of face-sharing octahedra.

In reference (7) a simple theory was proposed to explain such sinusoidal modulations as being due to the fact that the disorderly stacked ordered lamellae are not single layers, but consist of two layers of cations, the structure of the two layers being highly correlated. Such an assembly of two layers is present in our structure along the lamellae of face-sharing octahedra.

The same extinctions $hh0l$: $l = 2n$ and $000l$: $l = 2n$ were found in the electron diffraction patterns.

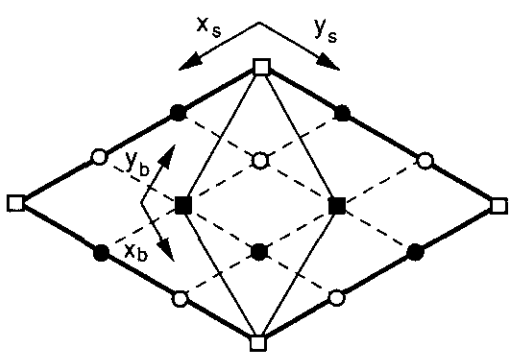

FIG. 2. Schematic representation of the $Ba_8Ta_4Ti_3O_{24}$ structure projected on (0001) plane. x_b–y_b represent the axes for the basic cell; x_s–y_s represent the axes for the superstructure cell. Squares correspond to the 00z positions in the basic cell; filled circles represent the 2/3, 1/3, z positions and empty circles represent the 1/3, 2/3, z positions in the basic cell.

3.3. *Crystal Structure of $Ba_8Ta_4Ti_3O_{24}$*

The coordinates of heavy atoms and the oxygen positions were determined starting from a model of close-packed BaO_3 layers, but taking into account the threefold superlattice cell. This approximation was judged satisfactory considering the good results of the structure refinement obtained for the basic structure. The refinement of the superstructure was carried out by the Rietveld method using an isotropic approximation for the thermal parameters (thermal parameters for all oxygen atoms were refined simultaneously). The experimental and crystallographic data are summarized in Table 1. Positional and thermal parameters and the main interatomic distances for the crystal structure of $Ba_8Ta_4Ti_3O_{24}$ are listed in Tables 2 and 3 respectively. Experimental, calculated, and difference X-ray patterns are shown in Fig. 4.

The crystal structure of $Ba_8Ta_4Ti_3O_{24}$ is the $8L$ $(cchc)_2$ close-packing of BaO_3 layers with overall symmetry $P6_3/mmc$. The presence of the superstructure changes the symmetry to $P6_3/mcm$.

The main features of the crystal structure deal with the distribution of the B-cations and of cation vacancies. There are two types of nonequivalent positions of the B-cations in octahedral interstices: in the chains of the corner-sharing octahedra and in the pairs of the FSO.

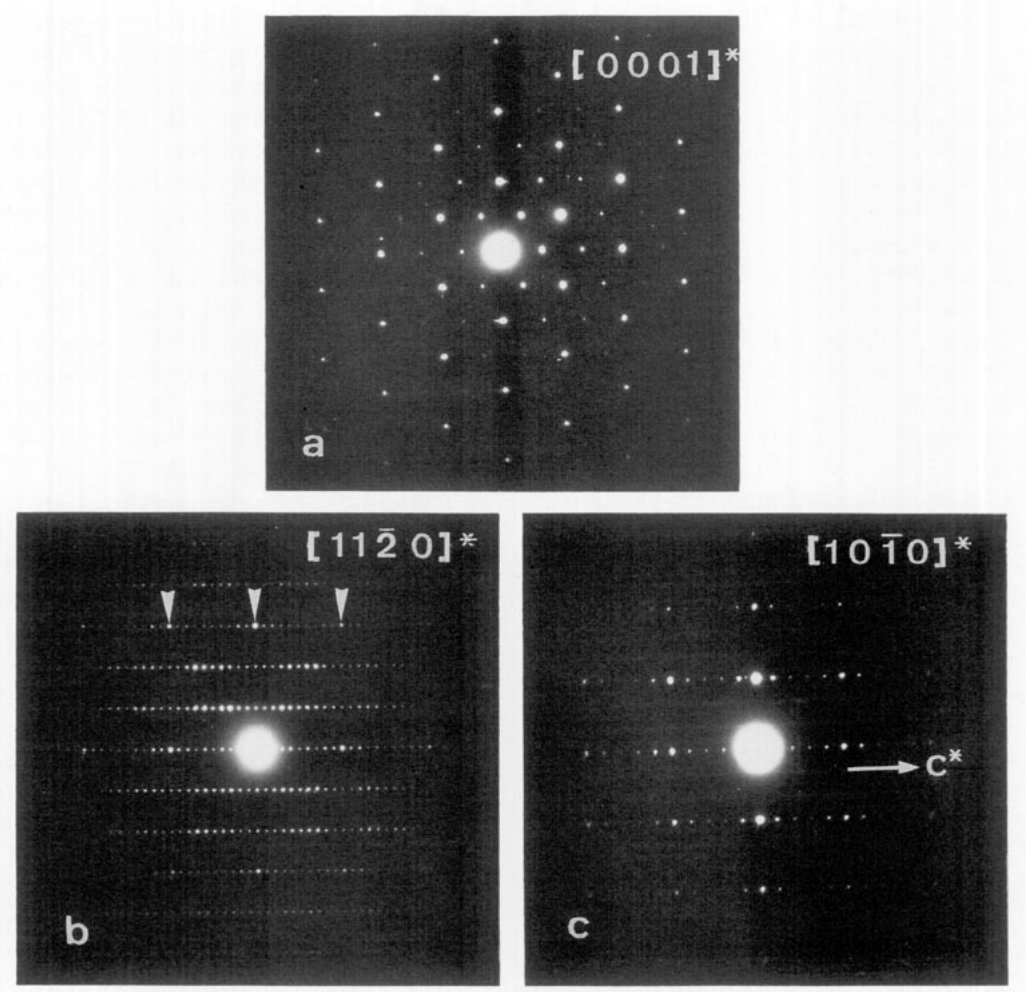

FIG. 3. Electron diffraction patterns for the $Ba_{10}Ta_{7.04}Ti_{1.2}O_{30}$ compound: (a) $[0001]_b^*$ zone; (b) $[11\bar{2}0]_b^*$ zone; (c) $[10\bar{1}0]_b^*$ zone. Note the similarities with the $Ba_8Ta_4Ti_3O_{24}$ compound; in the $[10\bar{1}0]_b^*$ zone streaks are present instead of superstructure spots.

TABLE 1
Crystallographic and Experimental Data for $Ba_8Ta_4Ti_3O_{24}$ and $Ba_{10}Ta_{7.04}Ti_{1.2}O_{30}$

	$Ba_8Ta_4Ti_3O_{24}$	$Ba_{10}Ta_{7.04}Ti_{1.2}O_{30}$
Space group	$P6_3/mcm$	$P6_3/mmc$
a (Å)	10.03144(5)	5.79806(4)
c (Å)	18.8694(2)	23.75473(3)
Z	3	1
V (Å^3)	1644.3	692.2
Calculated density (g/cm^3)	7.12	7.64
Radiation and wavelength	Cu$K\alpha_1$ λ = 1.54056 (Ge-mono)	
Diffractometer	Powder STADI/P, transmission mode	
Mode of refinement	Full profile	
Min and max 2θ	$4 \le 2\theta \le 115$	$62 \le \theta \le 115$
R_I, R_P, R_{wP}	0.041, 0.108, 0.094	0.039, 0.118, 0.099
Goodness of fit	0.25	0.29
Texture parameter along [001] axis	1.33(1)	1.48(1)

TABLE 2
Atomic Parameters for $Ba_8Ta_4Ti_3O_{24}$

Atom	Position	x/a	y/b	z/c	B_i (Å^2)
Ba1	2a	0	0	0	0.6(2)
Ba2	4d	1/3	2/3	0	2.1(2)
Ba3	6g	0.6596(8)	x	1/4	0.95(8)
Ba4	12k	0.6682(7)	0	0.3632(1)	1.83(5)
Ta1[a]	4e	0	0	0.1959(5)	0.7(2)
Ta2[b]	8h	1/3	2/3	0.1801(3)	1.3(2)
Ta3[c]	12k	0.3317(7)	0	0.4383(1)	0.70(5)
O1	12i	0.681(5)	0.179(4)	1/4	0.9(2)
O2	24l	0.498(3)	0.165(3)	0.1244(9)	0.9(2)
O3	12i	0.352(4)	$x/2$	1/2	0.9(2)
O4	12k	0.177(4)	0	0.111(2)	0.9(2)
O5	6g	0.143(6)	x	1/4	0.9(2)
O6	6f	1/2	0	0	0.9(2)

Note. Occupations: [a] 0.5Ta; [b] 0.25Ta + 0.625Ti; and [c] 0.667Ta + 0.333Ti.

TABLE 3
Main Interatomic Distances (Å) for $Ba_8Ta_3O_{24}$

Ba1–O3	3.06(4)	×6	Ba4–O1	2.72(2)	×2
Ba1–O4	2.75(3)	×6	Ba4–O5	2.86(4)	×1
Ba2–O3	2.73(4)	×3	Ba4–O2	2.90(3)	×2
Ba2–O2	2.89(2)	×6	Ba4–O4	2.93(1)	×2
Ba2–O6	2.896	×3	Ba4–O2	2.93(3)	×2
Ba3–O1	2.77(5)	×2	Ba4–O3	3.08(2)	×2
Ba3–O2	2.87(2)	×4	Ba4–O6	3.084(4)	×1
Ba3–O1	2.96(5)	×2			
Ba3–O5	2.97(6)	×2			
Ba3–O4	3.09(3)	×3			
Ta1–O5	1.76(4)	×3	Ta3–O4	1.81(4)	×1
Ta1–O4	2.39(3)	×3	Ta3–O3	2.04(3)	×2
Ta1–Ta1	2.04(1)	×1	Ta3–O2	2.04(2)	×2
Ta2–O2	1.99(3)	×3	Ta3–O6	2.050(6)	×1
Ta2–O1	2.09(3)	×3			
Ta2–Ta2	2.64(1)	×1			

The refinement of the occupancy (with fixed thermal parameters) for the position of *B*-cations in the corner-sharing octahedra (12*k*) gives an approximate value (2/3Ta + 1/3Ti). Therefore, further refinement was carried out with fixed occupancy for this position.

The increase of the unit cell size results in the separation of the crystallographic positions situated on the 00*z* axis of the basic cell (see Fig. 2). Consequently, there are two different positions in the centers of FSO in the $Ba_8Ta_4Ti_3O_{24}$ structure. It was found that the Ta1–Ta1 distance, i.e., between Ta atoms in adjacent FSO (4*e*-position) is very short, i.e., 2.04(1) Å. However, this result can be easily explained if one takes into account that only one of the pairs of octahedra is really occupied, the other one being empty. Indeed, the occupancy found for this position is (0.5Ta + 0.5□). This type of cation vacancy localization leads to a shift of the cations along the *c*-axis away from the centers of the octahedra toward the triangular face formed by the O5 atoms, which are shifted resulting in a Ta1–O5 bond length of 1.76 Å, while the O4 atoms are shifted to a Ta–O separation of 2.39 Å. As a consequence, the Ta1 atoms have a distorted coordination. The positions situated on the 1/3, 2/3, *z* and 2/3, 1/3, *z* axes are only partially occupied by (0.25Ta + 0.625Ti + 0.125□) and contain cation vacancies. Such a filling corresponds to the composition $Ba_8Ta_4Ti_3O_{24}$ which can be deduced from the known occupancies for the 12*k* and 4*e* positions. An increase in the average occupancy in these pairs of FSO influences the distance between

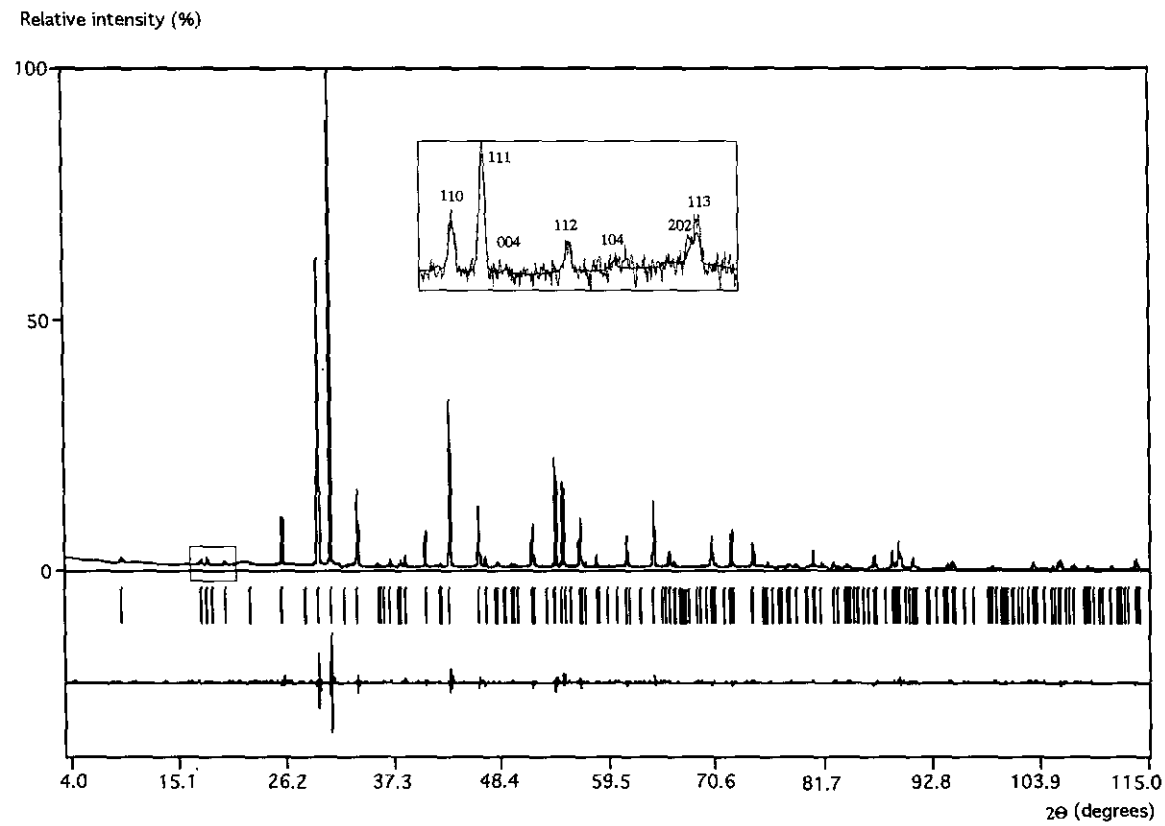

FIG. 4. Experimental and difference X-ray diffraction patterns for $Ba_8Ta_4Ti_3O_{24}$. Peak positions are marked only for the basic cell. Inset: peak positions and indices for the superstructure.

cations in their centers, which becomes 2.64 Å, and therefore the oxygen arrangement around the Ta2 atoms is close to ideal. A separation of 2.64 Å between the centers of these pairs of octahedra is still somewhat shorter than the Ti–Ti distance (2.67 Å) in the pairs of completely filled FSO in the hexagonal structure of $BaTiO_3$ oxide (8).

Atoms in corner-sharing octahedra have a slightly distorted octahedral oxygen coordination. The Ba atoms in the $Ba_8Ta_4Ti_3O_{24}$ structure have weakly distorted coordination polyhedra.

3.4. *The Crystal Structure of* $Ba_{10}Ta_{7.04}Ti_{1.2}O_{30}$

The crystal structure of $Ba_{10}Ta_{7.04}Ti_{1.2}O_{30}$ is based on the $10H$ $(hcccc)_2$ close-packing of BaO_3 layers along the c-axis. The refinement of the crystal structure was carried out only for the basic model (SG $P6_3/mmc$). Such an approximation is reasonable since no visible superstructure reflections were detected on the X-ray pattern of this compound. Moreover, the refinement of the superstructure led to the same values for the positional and thermal parameters of the atoms. The refinement of the crystal structure in an isotropic approximation for the thermal parameters led to the following values of the R factors: $R_I = 0.039$, $R_P = 0.118$, and $R_{wP} = 0.099$. Experimental and crystallographic data are summarized in Table 1. Positional and thermal parameters and main interatomic distances for the crystal structure of $Ba_{10}Ta_{7.04}Ti_{1.2}O_{30}$ are listed in Tables 4, and 5 respectively. Experimental, calculated, and difference X-ray diffraction patterns are shown in Fig. 5.

The crystal structure of $Ba_{10}Ta_{7.04}Ti_{1.2}O_{30}$ is very closely related to that of $Ba_8Ta_4Ti_3O_{24}$ but is more disordered as shown by the electron diffraction study.

In the crystal structure of $Ba_{10}Ta_{7.04}Ti_{1.2}O_{30}$ two types of corner-sharing ocathedra are present. All of them are jointly occupied by Ta and Ti atoms. Assuming the cation vacancies to be situated in FSO the occupancies of the corner-shared octahedra were refined with fixed thermal parameters. The octahedra with centers in the $4f$ and the $2a$ positions have the occupancy (0.9Ta + 0.1Ti). In this structure Ta2 atoms have considerably distorted oxygen coordinations, while Ta1 atoms are situated in ideal octahedra.

The structure contains only one type of FSO with centers in the $4f$ position. In this case the Ta3–Ta3 distance is 2.34 Å. This short distance also results in a considerable distortion of the coordination polyhedra for these atoms, which leads to a Ta3–O1 bond length of 1.95 Å, while a Ta3–O3 distance is 2.25 Å. Assuming the overall composition to be known, the occupancy of this position is (0.41Ta + 0.15Ti + 0.44□). The refinement of the anisotropic thermal parameters for B-cations revealed a strong anisotropy (B_{11} = 1.0(2) Å^2, B_{33} = 2.5(3) Å^2) for Ta3 atoms, while Ta1 and Ta2 have practically isotropic thermal parameters.

The basic structures for both $Ba_8Ta_4Ti_3O_{24}$ and $Ba_{10}Ta_{7.04}Ti_{1.2}O_{30}$ compounds are shown in Fig. 6.

3.5. *High-Resolution Electron Microscopy Study (HREM)*

3.5.1. Perfectly ordered structures. HREM images were obtained along the most relevant zones of the hexagonal structure: $[10\bar{1}0]$ and $[11\bar{2}0]$. Figures 7 and 8 show the high resolution images of $Ba_8Ta_4Ti_3O_{24}$ and $Ba_{10}Ta_{7.04}Ti_{1.2}O_{30}$ respectively.

Along the $[10\bar{1}0]$ zone the structure is viewed parallel to the close-packed rows of · · ·O–Ba–O–Ba· · ·; it directly reveals the stacking of the close-packed BaO_3 layers. The bright dots of Fig. 7a can be interpreted as the images of the · · ·O–Ba–O–Ba· · · columns. This is supported by the image simulations (Figures 9 and 10). The most striking feature is the "fish-bone" configuration of the rows of bright dots, rows characteristic of a periodic polysynthetically twinned structure. The number of rows of bright dots parallel to the twin interface in one band is 4 in $Ba_8Ta_4Ti_3O_{24}$ and 5 in $Ba_{10}Ta_{7.04}Ti_{1.2}O_{30}$, corresponding to the number of BaO_3 layers. The c-parameters 18.86 and 23.75 Å are clearly determined by the period of this twinned texture. The present structures are striking

TABLE 4
Atomic Parameters for $Ba_{10}Ta_{7.04}Ti_{1.2}O_{30}$

Atom	Position	x/a	y/b	z/c	B_i (Å^2)
Ba1	$2d$	2/3	1/3	1/4	1.1(1)
Ba2	$4e$	0	0	0.3390(2)	1.9(1)
Ba3	$4f$	2/3	1/3	0.5539(1)	1.32(9)
Ta1[a]	$2a$	0	0	0	1.2(1)
Ta2[a]	$4f$	2/3	1/3	0.3989(1)	1.9(1)
Ta3[b]	$4f$	2/3	1/3	0.7992(2)	0.5(1)
O1	$6h$	0.817(2)	$-x$	3/4	1.6(5)
O2	$12k$	0.325(3)	$1/2x$	0.4522(7)	0.8(3)
O3	$12k$	0.495(2)	$2x$	0.6443(6)	2.4(4)

Note. Occupations: [a] 0.9Ta + 0.1Ti; [b] 0.41Ta + 0.15Ti.

TABLE 5
Main Interatomic Distances (Å) for $Ba_{10}Ta_{7.04}Ti_{1.2}O_{30}$

Ba1–O1	2.91(1)	×6	Ba3–O2	2.96(2)	×3
Ba1–O3	2.99(1)	×6	Ba3–O2	2.90(2)	×3
Ba2–O1	2.80(1)	×3	Ba3–O3	2.76(1)	×6
Ba2–O2	3.15(2)	×3			
Ba2–O3	2.93(1)	×6			
Ta1–O2	1.99(2)	×6	Ta3–O1	1.91(1)	×3
Ta2–O2	2.13(2)	×3	Ta3–O3	2.19(1)	×3
Ta2–O3	1.86(1)	×3	Ta3–Ta3	2.337(7)	×1

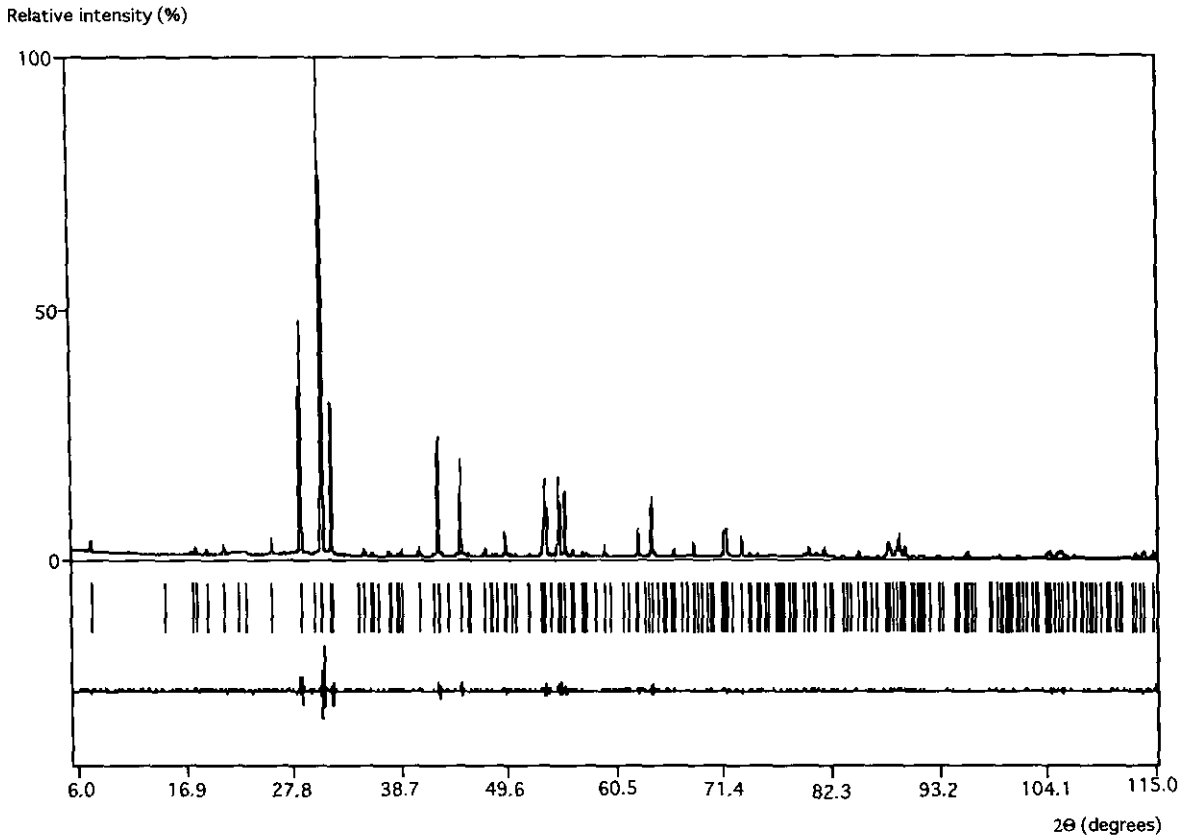

FIG. 5. Experimental and difference X-ray diffraction patterns for $Ba_{10}Ta_{7.04}Ti_{1.2}O_{30}$.

examples of sub-unit-cell twinning (9). In the thinnest parts, weak dots are observed in the centers of the parallelograms formed by the brightest dots; they image the rows of *B*-cations in the octahedral interstices of the BaO_3 layers.

The [11$\bar{2}$0] zone of Fig. 7b is parallel to the edges of the superlattice unit cell in the $Ba_8Ta_4Ti_3O_{24}$ compound; in this direction the centers of crystallographically equivalent FSO are aligned and form columns. The period of the succession of columns corresponds to the long diagonal of the superlattice unit mesh and there are three rows of occupied octahedra in this period. This period can be seen in the image of Fig. 7b. It is consistent with the tripling of the period observed in electron diffraction (Fig. 1c). The quality of the image is not perfect because the material is rather sensitive to 400 keV electron radiation. The period is nevertheless marked by extra bright (or dark) dots in Fig. 7b. The superperiod in the image can be revealed more clearly by producing an optical diffraction pattern of the high resolution negative. Such a diffraction pattern is reproduced as inset in Fig. 7b, and can be compared with the electron diffraction pattern of Fig. 1c.

The radiation sensitivity of the ordered $Ba_8Ta_4Ti_3O_{24}$ structure is consistent with our ordering model which attributes the order to vacancies in the lamellae of FSO. It is well established that vacancy ordered structures are very sensitive to radiation damage because of the presence of these structural vacancies. The radiation disordering is only clearly visible in the zone which reveals the superstructure. Also in the electron diffraction pattern along this zone the superstructure spots weaken rapidly under the electron beam intensity needed for high resolution imaging.

The HREM image along the [11$\bar{2}$0] zone of the $Ba_{10}Ta_{7.04}Ti_{1.2}O_{30}$ compound is reproduced in Fig. 8b. As compared to Fig. 7b which refers to $Ba_8Ta_4Ti_3O_{24}$ the superstructure is restricted to small areas. This is consistent with the corresponding electron diffraction pattern (Fig. 3c) which exhibits streaks instead of spots at the positions $h = 3n$. These effects result from the disordered occupation of the FSO.

3.5.2. Image simulations. In support of the interpretation of the high resolution observations along the [10$\bar{1}$0] zone axis, images were simulated for both compounds, using the "Mac Tempas" software package. The coordinates and occupancies determined by X-ray diffraction were used as input. The origin in the left bottom corner of the frame corresponds to the position of a Ba–O–Ba

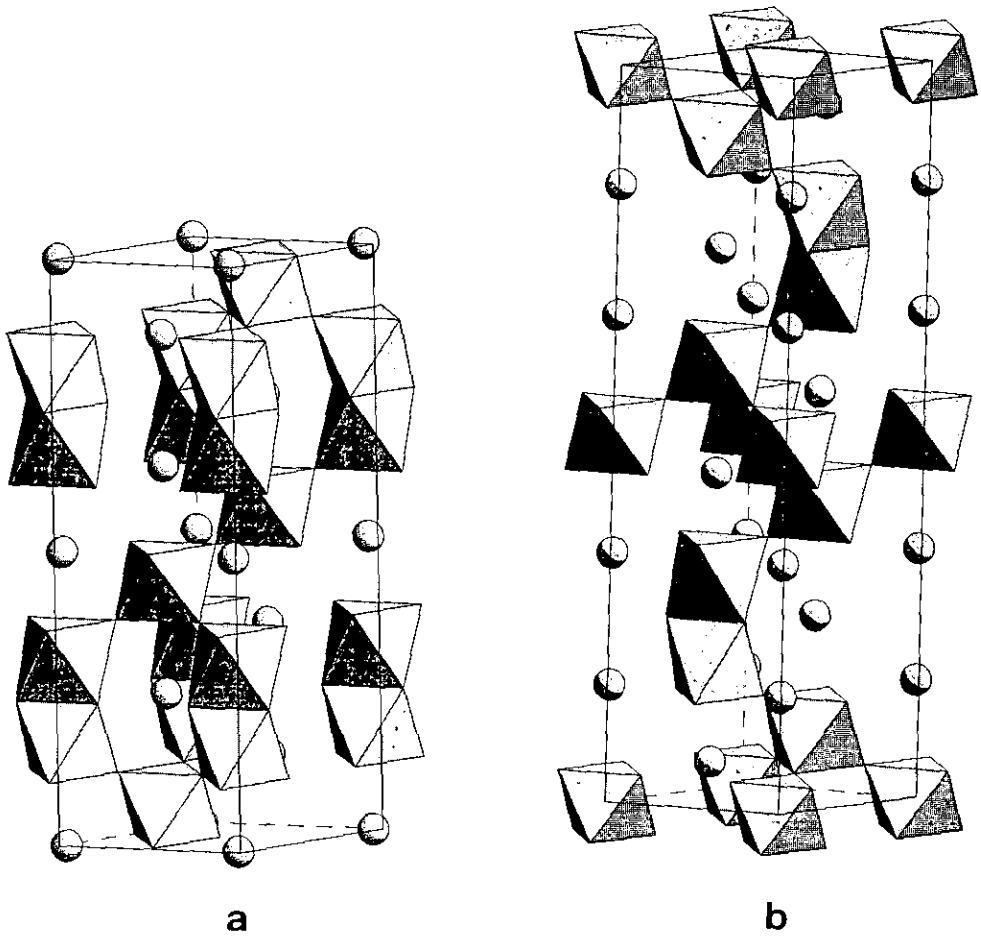

FIG. 6. Representation of the basic structures for (a) $Ba_8Ta_4Ti_3O_{24}$ and (b) $Ba_{10}Ta_{7.04}Ti_{1.2}O_{30}$ deduced from the X-ray diffraction data. Spheres represent Ba atoms.

close-packed row in the $Ba_8Ta_4Ti_3O_{24}$ images, and to a Ta position in the $Ba_{10}Ta_{7.04}Ti_{1.2}O_{30}$ compound.

Images were obtained for several relevant thicknesses and for defocus values in the vicinity of Scherzer defocus. The results are shown in Fig. 9a for the $Ba_8Ta_4Ti_3O_{24}$ and in Fig. 10 for the $Ba_{10}Ta_{7.04}Ti_{1.2}O_{30}$ compound.

In the $Ba_8Ta_4Ti_3O_{24}$ images the less bright dots have two different levels of brightness. In an oblique row of four, the two outer ones are less bright than the two inner ones, corresponding respectively to the face-sharing and the corner-sharing octahedral sites. Certain areas of the experimental images of the $Ba_8Ta_4Ti_3O_{24}$ compound exhibit such a behavior; this is for instance visible in the highly magnified image of Fig. 9b, it confirms in a striking manner the results of the structure determination.

Also in the $Ba_{10}Ta_{7.04}Ti_{1.2}O_{30}$ image the most prominent bright dots correspond to the BaO_3 framework. The sequences of five less bright dots along the oblique rows image the *B*-cations. This is again consistent with the structure model and is confirmed by the experimental images.

3.5.3. Defects. The simplest type of defect occurring in these materials is the presence of singular twin bands with different widths. Figure 11 shows a region of the $Ba_8Ta_4Ti_3O_{24}$ compound containing two singular bands (indicated by arrows), of five layers instead of four. Such a band can be considered as half a unit cell of the $Ba_{10}Ta_{7.04}Ti_{1.2}O_{30}$ structure. The reverse is also observed i.e., a singular band of $Ba_8Ta_4Ti_3O_{24}$, in a matrix of $Ba_{10}Ta_{7.04}Ti_{1.2}O_{30}$ (Fig. 12). These observations illustrate the close relationship between the structures of the two phases. It suggests that for compositions which are intermediate between that of $Ba_{10}Ta_{7.04}Ti_{1.2}O_{30}$ the structure of which can be represented by the symbol 55, and that of $Ba_8Ta_4Ti_3O_{24}$ (represented by 44), more complicated regular sequences such as . . .45.45. . . or . . .445.445. . . could arise.

The HREM image of Fig. 13 shows a singular five layer band embedded in the $Ba_8Ta_4Ti_3O_{24}$ compound. One BaO_3 layer is interchanged between the five layer band and the adjacent four layer band, causing a step in the twin interface (Fig. 14). This step is equivalent to a twinning

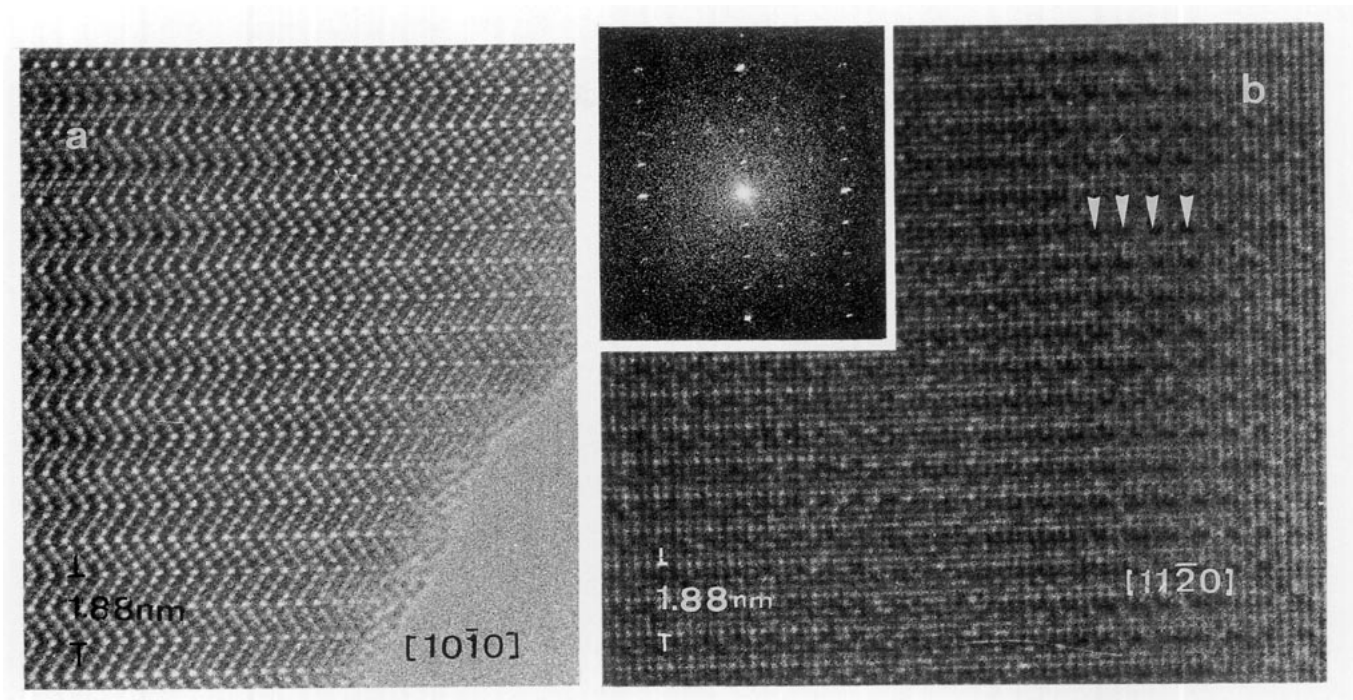

FIG. 7. HREM images of $Ba_8Ta_4Ti_3O_{24}$: (a) along the [10$\bar{1}$0] zone; bright dots represent Ba–O–Ba–O columns, less bright dots the *B*-cation columns; (b) along the [11$\bar{2}$0] zone; the superstructure dots are indicated by arrows. Inset: Optical diffraction pattern of the microscopic image showing the superstructure spots; it can be compared with the electron diffraction pattern of Fig. 1c.

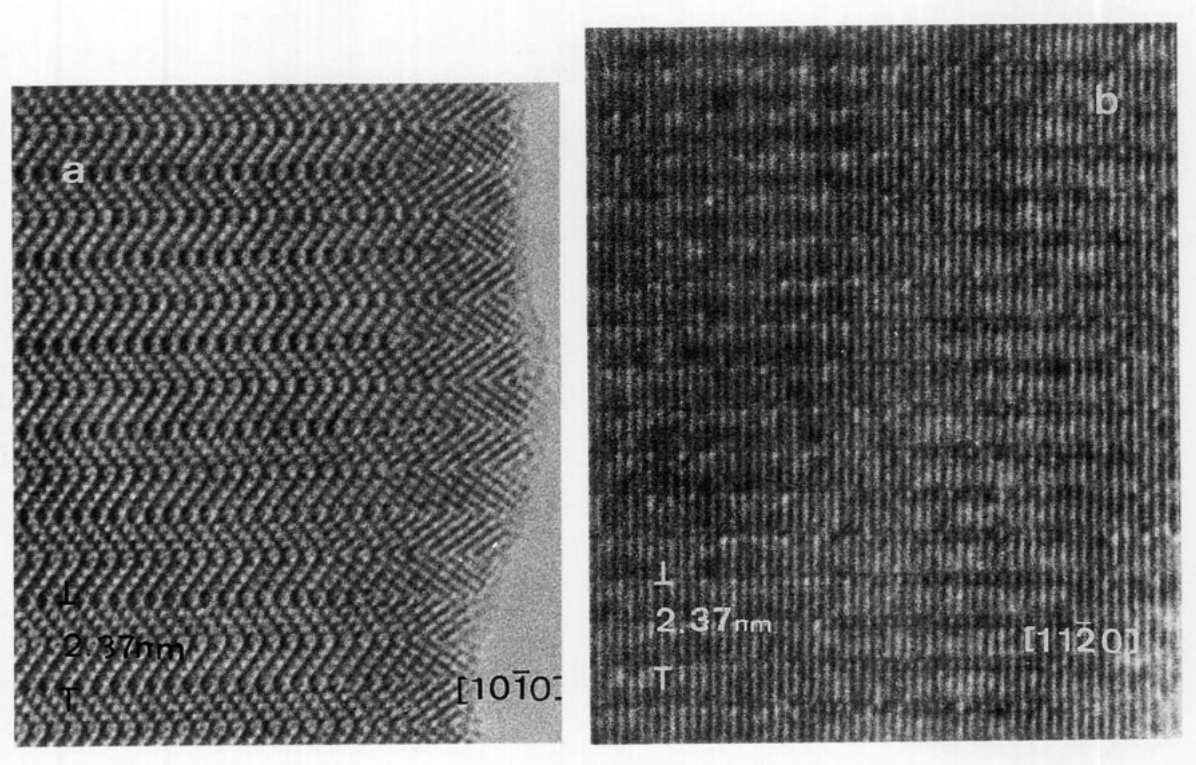

FIG. 8. HREM images of $Ba_{10}Ta_{7.04}Ti_{1.2}O_{30}$: (a) along the [10$\bar{1}$0] zone; bright dots represent Ba columns, darker dots the *B*-cation columns; (b) along the [11$\bar{2}$0] zone. Note the mottled contrast of the superstructure dots in very restricted areas.

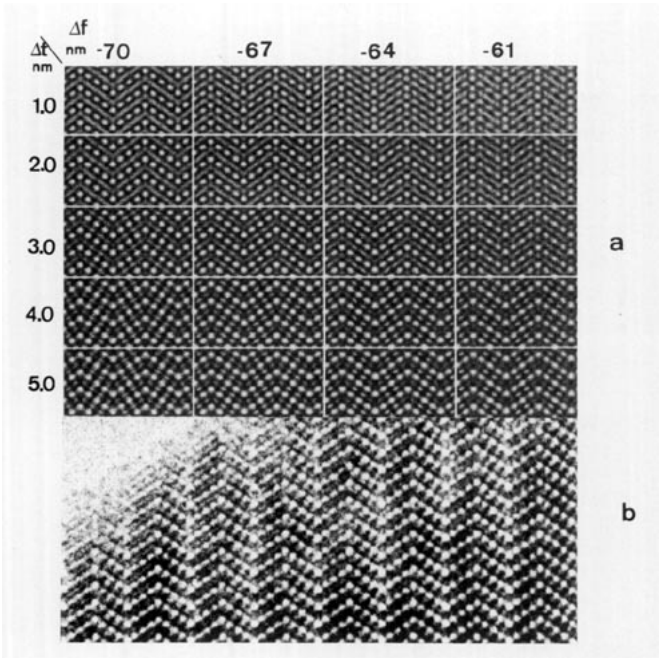

FIG. 9. (a) Matrix of calculated high resolution images along the close-packed direction of $Ba_8Ta_4Ti_3O_{24}$ for different defocus values (horizontal) and different thicknesses (vertical); C_s = 1 mm, θ = 0.55 mrad; (b) HREM image in the thinnest part of the sample for comparison.

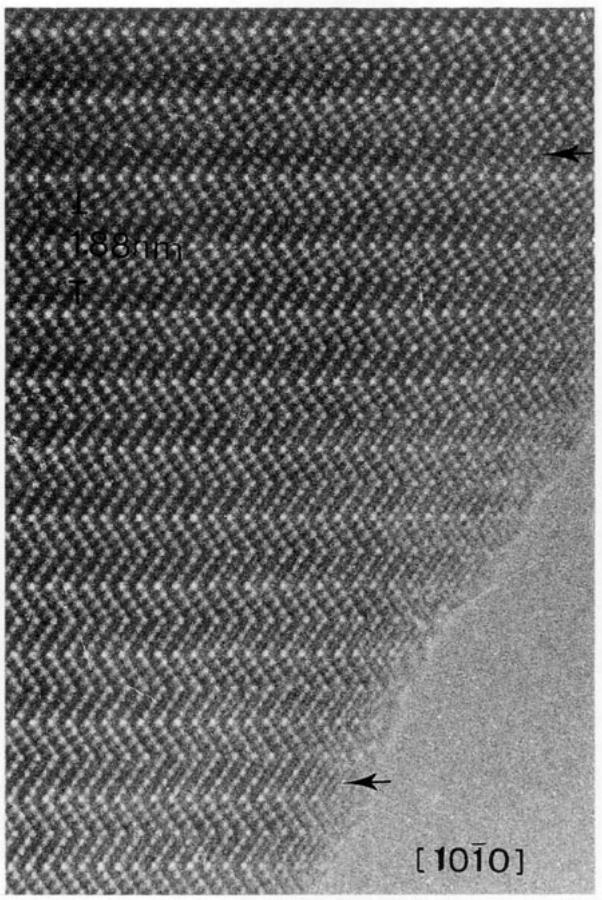

FIG. 11. HREM image of $Ba_8Ta_4Ti_3O_{24}$ showing bands (indicated by arrows) of half lamella of $Ba_{10}Ta_{7.04}Ti_{1.2}O_{30}$ inserted in the $Ba_8Ta_4Ti_3O_{24}$ structure.

dislocation. The propagation of such a dislocation along the twin interface widens the four layer band at the expense of the five layer band. The motion of the dislocation occurs by glide along the close-packed planes accompanied by jumping of the *B*-cations, i.e., by a synchro-shear process (10). The glide motion changes the close-packed stacking mode. It transforms one layer of face-sharing octahedra into a layer of corner-sharing octahedra or vice versa. This must be accompanied by jumping of a *B*-cation from a face-sharing octahedron into a corner-sharing octahedron and vice versa in order to maintain the same coordination.

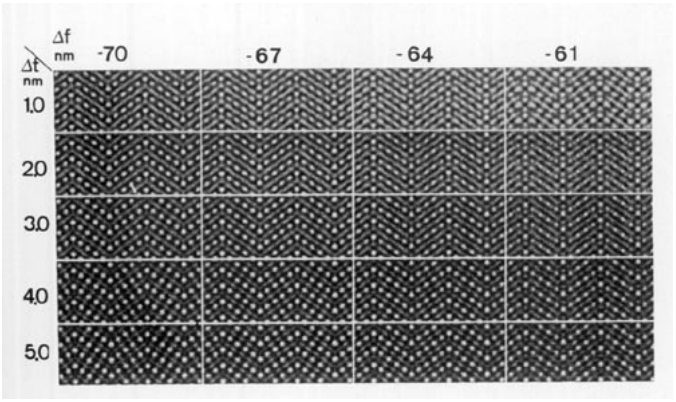

FIG. 10. (a) Matrix of calculated high resolution images along the [10$\bar{1}$0] zone of $Ba_{10}Ta_{7.04}Ti_{1.2}O_{30}$ for different defocus values (horizontal) and different thicknesses (vertical); C_s = 1 mm, θ = 0.55 mrad.

Figure 12 shows a crystal fragment of the $Ba_{10}Ta_{7.04}Ti_{1.2}O_{30}$ compound. Bands of the $Ba_8Ta_4Ti_3O_{24}$ structure, indicated by arrows, are also present. Moreover the area contains an intrinsic stacking fault (indicated by a big arrow) separating two $Ba_{10}Ta_{7.04}Ti_{1.2}O_{30}$ bands having the same orientation. The schematic of this fault is presented in Fig. 15. The occurrence of such a fault implies the presence of a lamella—*chhc* of three layers of FSO. It seems reasonable to assume that the presence of this fault allows accommodation of vacancies in the central layer and higher changed tantalum ions in the adjacent layers of octahedral sites. In this sense the stacking fault plays the same role as the twin interfaces in accommodating highly charged ions and vacancies. A similar structural feature was found in the compounds belonging to the homologous series $La_nTi_{n-1}O_{3n}$ (11), which have structures based on the close-packed stacking of LaO_3 layers. In the latter case the superperiod is due to the

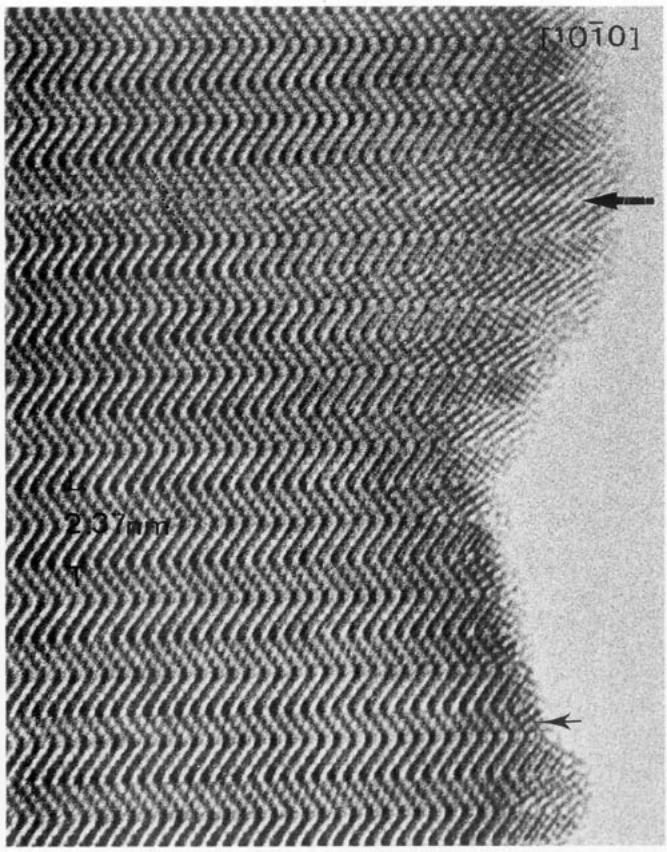

FIG. 12. HREM image showing defects in the $Ba_{10}Ta_{7.04}Ti_{1.2}O_{30}$ compound. The small arrow indicates the insertion of a half $Ba_8Ta_4Ti_3O_{24}$ lamella. The large arrow indicates the defect illustrated schematically in Fig. 15.

periodic arrangement of such faults, which accommodate vacancies in the titanium sublattice.

4. DISCUSSION

Summarizing the results of X-ray and electron microscopy investigations one can conclude that the crystal structures of both $Ba_{10}Ta_{7.04}Ti_{1.2}O_{30}$ and $Ba_8Ta_4Ti_3O_{24}$ are closely related. However the first is less ordered and probably also contains different types of FSO which occur disorderly in the crystal structure. Complete ordering of the cations in FSO should lead either to a superlattice formation or to a decrease of the symmetry of the structure. In the first case superlattice spots such as those observed in $Ba_8Ta_4Ti_3O_{24}$ should be present. In the second case neither streaks nor superlattice spots would be observed in electron diffraction, but the diffraction conditions might be changed as a consequence of the loss of symmetry elements. The results of the structure refinement which led to a Ta–Ta distance of 2.33 Å indirectly support the assumption of a partial order in $Ba_{10}Ta_{7.04}Ti_{1.2}O_{30}$ as concluded from the presence of streaks. The observed Ta–Ta distance in FSO is in fact the average of the Ta–Ta distances observed in the two types of FSO in $Ba_8Ta_4Ti_3O_{24}$ (2.04 and 2.64 Å). Also the anisotropy of the thermal parameter for Ta3 atoms suggests the presence of two Ta–Ta distances i.e., two types of FSO in a disordered manner leading to incipient split positions for Ta.

The formation of $Ba_8Ta_{4.64-x}Ti_{2.2+x}O_{24-x/2}$ solid solutions was not observed. This means that the composition of the BaO_3 layers is constant and does not depend on the composition of the *B*-framework. Such a conclusion is also supported by the existence of a very stable octahedral arrangement for Ta^{5+} and Ti^{4+} ions and consequently the impossibility of oxygen vacancies localization. Therefore the ratios of Ta : Ti cations is determined only by oxygen stoichiometry.

Since the charge balance requires that four Ta^{5+} ions should be replaced by five Ti^{4+} general the formula for the solid solutions $Ba_{10}Ta_{8-0.8x}Ti_xO_{30}$ and $Ba_8Ta_{4+0.8x}Ti_{3-x}O_{24}$ can be written as $Ba_5(Ta, Ti)_{4+\delta}O_{15}$ or $A_nB_{n-1+\delta}O_{3n}$. In the series: $Ba_5Ta_4O_{15} \rightarrow Ba_{10}Ta_{8-0.8x}Ti_xO_{30} \rightarrow Ba_8Ta_{4+0.8x}Ti_{3-x}O_{24} \rightarrow BaTiO_3$ the value of δ increases with increasing titanium content.

It was found empirically that the type of close-packing

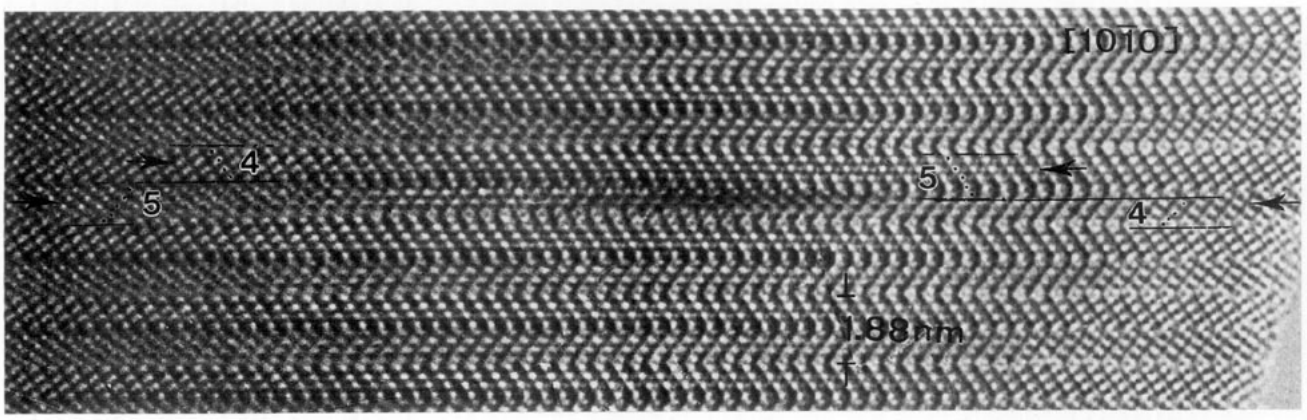

FIG. 13. HREM image illustrating a twinning dislocation in $Ba_8Ta_4Ti_3O_{24}$. The alternation of packing of BaO_3 layers along the defect is illustrated.

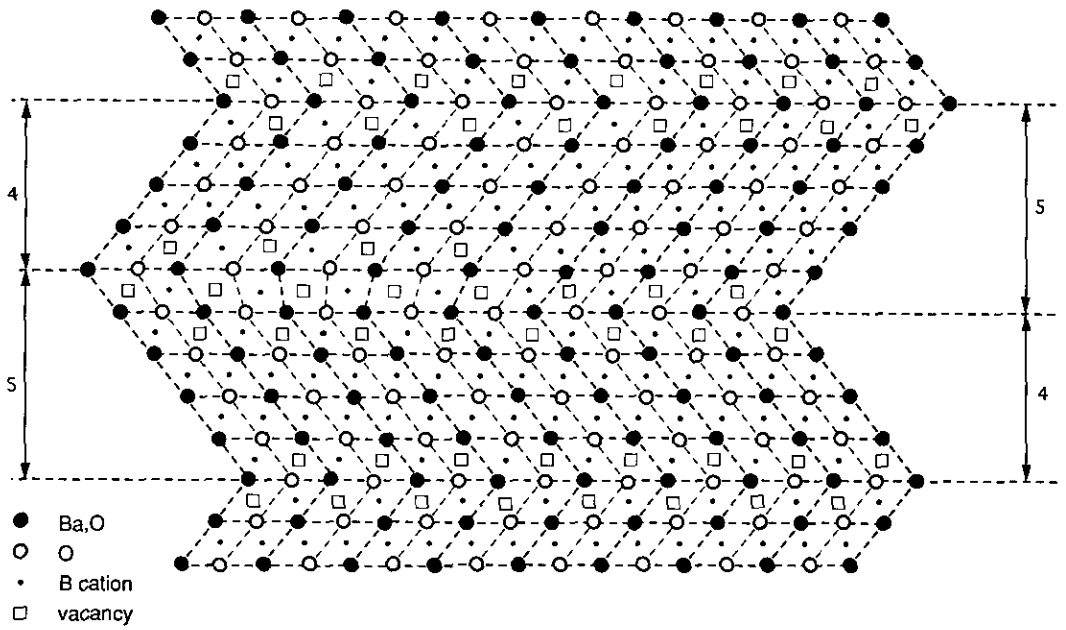

FIG. 14. Model of the defect imaged in Fig. 13. Note the step in the twin interface caused by the presence of a twinning dislocation.

of BaO_3 layers depends on δ, which is itself determined by the Ti concentration. $\delta = 0$ corresponds to the $Ba_5Ta_4O_{15}$ oxide, which has a trigonal structure based on a five-layer sequence of close packed layers described by the stacking symbol (*hccch*) and the space group $P\bar{3}m1$ (12). The main feature of the $Ba_5Ta_4O_{15}$ structure is the presence of chains of three face-sharing octahedra, cation vacancies being located in the central layer of octahedra and Ta ions in the other ones, since this assures the largest separation of Ta^{5+} ions.

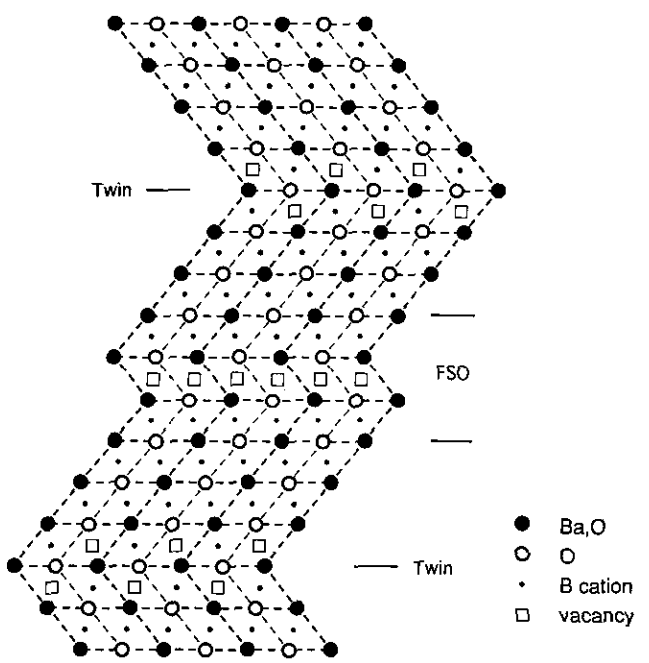

FIG. 15. Model of the defect imaged in Fig. 12. The defect is an intrinsic stacking fault.

For $\delta > 0$, as would be the case if Ta is replaced by Ti in the (*hccch*) framework, certain Ti ions would have to occupy sites which were vacant if $\delta = 0$. In this case extremely short metal–metal separations would result and cause a large repulsion between the highly charged *B*-cations. This can be avoided by adopting a different close packed framework in which less FSO occur than in *hccch*; such a framework is obtained in the $(cchcc)_2$ stacking, which occurs in the $Ba_{10}Ta_{8-0.8x}Ti_xO_{30}$ structure. This change in the framework stacking is accompanied by a "delocalization" of the cation vacancies. The vacancies can partly occupy positions in the pairs of FSO, the remaining positions being occupied by *B*-cations. Such an arrangement results in a reduction of the electrostatic repulsion.

We found that a series of solid solutions $Ba_{5-x}La_xTa_{4-x}Ti_xO_{15}$ with a $Ba_5Ta_4O_{15}$ type of structure exists at least up to $x = 2$. The partial substitution of Ba by La allows the oxygen composition to remain constant and hence to maintain a close packed (Ba, La)O_3 framework in which the *B*-cations are located. The number of cation vacancies does not depend on x in this case ($\delta = 0$), since the charge unbalance created by replacing Ta^{5+} by Ti^{4+} is compensated for by the simultaneous substitution of Ba^{2+} by La^{3+}.

As a semiquantitative measure of the electrostatic en-

ergy and hence for the stability of various structures one can use Madelung's constant. The dependence of Madelung's constant on x has been computed using Ewald's method of convergent series using an algorithm described in (13). The charges associated with statistially occupied positions were chosen to be equal to a weighted average, the site occupancies being used as weighting factors. Since the lattice parameters are only weakly dependent on x, they were assumed to be constant and equal to their smallest value. The calculations were carried out for two series of solid solutions:

(i) the series $Ba_{10}Ta_{8-0.8x}Ti_xO_{30}$ with $(cchcc)_2$ layer stacking;

(ii) the hypothetical series $Ba_5Ta_{4-0.8x}Ti_xO_{15}$ with $(hccch)$ layer stacking.

In the last series we have assumed that the solid solution is generated by inserting Ti atoms in the central layer of octahedra, which is completely vacant in $Ba_5Ta_4O_{15}$. In the case of the (i) series, the calculations were carried out with the assumption that the substitution of Ta^{5+} by Ti^{4+} occurs only in corner-sharing octahedra. The replacement of Ta5+ by Ti4+ in a ratio 4 : 5 only in FSO would not change the average charge of B-cations in these positions and consequently the Madelung's constant would remain constant. It was found that the rate of decrease of Madelung's constant with x is quite different for the two cases (Fig. 16). For the hypothetical (ii) series of which the close packed BaO_3 layers contain $chhc$ lamellae (cc intrinsic stacking faults), the slope is found to be much larger than for the (i) series which contain lamellae having the chc stacking mode, i.e., which contain twin interfaces in their BaO_3 matrix. This difference in behavior suggests that the chc stacking is more stable as compared with the $chhc$ stacking, with respect to aliovalent substitution in the B-cations sublattice. This result also shows that the solid solutions for (ii) series cannot be formed, and any increase in δ should lead to a change in the type of close-packing.

Heterovalent substitution of Ta^{5+} by Ti^{4+} in $Ba_5Ta_4O_{15}$ results in the formation of the $10H$ close-packing. In the $Ba_{10}Ta_{7.04}Ti_{1.2}O_{30}$ compound the average occupancies for the two types of FSO are very close: (0.5Ta + 0.5□) and (0.56(Ta, Ti) + 0.44□). This similarity of occupancies creates a possibility for disordered arrangement of different pairs of FSO. However, high resolution images of $Ba_{10}Ta_{7.04}Ti_{1.2}O_{30}$ oxides revealed small areas where an ordered structure was observed. This fact is confirmed also by the presence of spots on the streaks which have been seen on some of the electron diffraction patterns of the [1010]* zone. In principle, complete ordering may occur after an appropriate thermal treatment.

Further decreasing the number of cation vacancies results in the rise of the average occupancy in the second type of FSO. As has been shown, in the $Ba_8Ta_4Ti_3O_{24}$ compound it is (0.875(Ta, Ti) + 0.125□), which essentially differs from the occupancy in the first type of FSO (0.5Ta + 0.5□). As a consequence the possibility for the formation of ordered phases appears. Such an ordering is realized in the structure with $8H$ close-packing. The increase in occupancy in the second type of FSO cannot occur, since no evidence of the existence of $Ba_8Ta_{4+0.8x}Ti_{3-x}O_{24}$ ($x < 0$) solid solutions was found. In

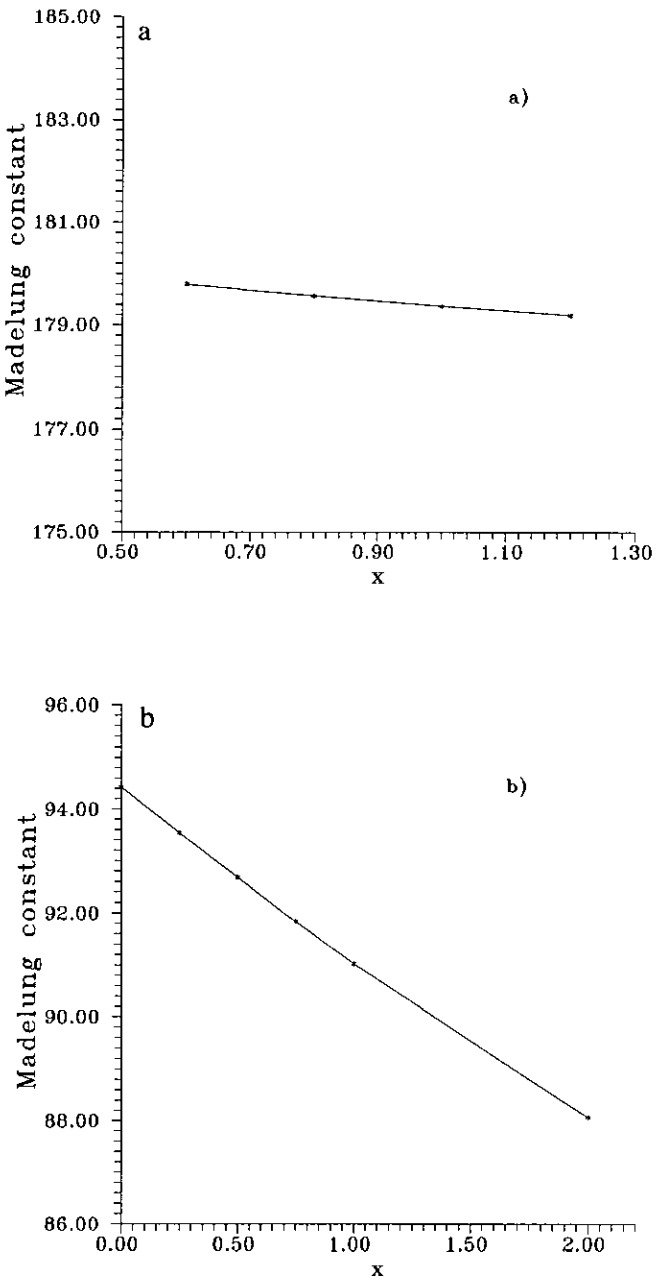

FIG. 16. Dependence of Madelung's constant on x for solid solutions: (a) $Ba_{10}Ta_{8-0.8x}Ti_xO_{30}$; (b) $Ba_5Ta_{4-0.8x}Ti_xO_{15}$.

this case two-phase samples were obtained with a cubic $BaTiO_3$ oxide. The structure of the last one contains only chains of corner-sharing octahedra.

The crystal structure of the complex $Ba_8Ta_4Ti_3O_{24}$ oxide is the first example of a cation-deficient hexagonal perovskite having such a distribution of *B*-cations and vacancies. FSO partially occupied by tungsten ions and vacancies ($0.677W + 0.333\square$) were found earlier in $Ba_2W_3O_9$, but in that case all these octahedra are crystallographically equivalent (14). The structure of the compound $Ba_8Nb_4Ti_3O_{24}$ was also studied in (4), but evidence was presented neither for the occurrence of a superstructure nor for the presence of two types of FSO. However, it may be possible that this compound has the same structure as $Ba_8Ta_4Ti_3O_{24}$.

These results suggest that more complex structures can be realized for the known compounds $Ba_4M_3LiO_{12}$ (M = Ta, Nb) (2) or $Ba_5W_3Li_2O_{15}$ (3). In these structures the experimentally observed distances between the *B*-cations in FSO are 2.258 and 2.198 Å respectively. We can assume that at least two different types of FSO may exist, so these short distances could be considered average ones in the different types of FSO. Moreover, in the crystal structures of $Ba_4Ru_3MO_{12}$ (M = Na, Li) (15) and $Ba_3MRu_2O_9$ (M = Zn, Ni) (16) the formation of two types of FSO is impossible, since the reduction of the electrostatic repulsion is achieved by the occurrence of Ru–Ru bonds. In the latter case the distances between Ru atoms situated in adjacent octahedra are about 2.7 Å.

ACKNOWLEDGMENTS

One of us (L.N.) thanks Thomas Krekels for help in performing the high resolution imaging. This text presents research results of the Belgian Programme on InterUniversity Poles of Attraction initiated by the Belgian State, Prime Ministers Office of Science Policy Programming. Scientific responsibility is assumed by the authors. The Russian Science Foundation is acknowledged for its financial support.

REFERENCES

1. P. C. Donohue, L. Katz, and R. Ward, *Inorg. Chem.* **43,** 306 (1965).
2. B. M. Collins, A. J. Jacobson, and B. E. F. Fender, *J. Solid State Chem.* **10,** 29 (1974).
3. A. J. Jacobson, B. M. Collins, and B. E. F. Fender, *Acta Crystallogr. Sect. B* **30,** 816 (1974).
4. B. Mössner and S. Kemmler-Sack, *J. Less-Common Met.* **120,** 203 (1986).
5. L. G. Akselrud, Yu. N. Gryn, P. U. Zavalij, V. K. Pecharsky, and V. S. Fundamentsky, Thes. Report, 12th European Crystallographic Meeting, Moscow, 1989, p. 155.
6. D. Van Dyck, D. Colaitis, and S. Amelinckx, *Phys. Status Solidi A* **68,** 385 (1981); D. Colaitis, D. Van Dyck, and S. Amelinckx, *Phys. Status Solidi A* **68,** 419 (1981).
7. M. Verwerft, G. Van Tendeloo, J. Van Landuyt, and S. Amelinckx, *Appl. Phys. A* **51,** 332 (1990).
8. R. D. Burbank and H. T. Evans, *Acta Crystallogr.* **1,** 330 (1948).
9. G. Van Tendeloo, D. Van Dyck, S. Kuypers, and S. Amelinckx, *Phys. Status Solidi A* **101,** 339 (1987); G. Van Tendeloo, D. Van Dyck, S. Kuypers, H. W. Zandbergen, and S. Amelinckx, *Phys. Status Solidi A* **102,** 597 (1987).
10. M. L. Kronberg, *Acta Metall.* **9,** 970 (1961).
11. G. Van Tendeloo, S. Amelinckx, B. Barriet, R. Bontchev, J. Darriet, and F. Weill, *J. Solid State Chem.* **108,** 336 (1994).
12. J. Shannon and L. Katz, *Acta Crystallogr. Sect. B* **26,** 102 (1970).
13. S. G. Popov and V. A. Levitskiy, *Zh. Fiz. Khim.* **LV,** 87 (1981). [Russian]
14. K. R. Poeppelmeier, A. J. Jacobson, and J. M. Longo, *Mater. Res. Bull.* **15,** 339 (1980).
15. P. D. Battle, S. H. Kim, and A. V. Powell, *J. Solid State Chem.* **101,** 161 (1992).
16. P. Lightfoot and P. D. Battle, *J. Solid State Chem.* **89,** 174 (1990).